



Synergetic combustion behavior of aluminum and coal addition in hybrid iron-methane-air premixed flames

Yueh-Heng Li^{a,*}, Stalline Pangestu^a, Aris Purwanto^a, Chih-Ting Chen^{a,b}

^a Department of Aeronautics and Astronautics, National Cheng Kung University, Tainan 701, Taiwan, ROC

^b Department of Biomedical Engineering, Johns Hopkins University, Baltimore, Maryland, USA



ARTICLE INFO

Article history:

Received 31 July 2020

Revised 10 February 2021

Accepted 11 February 2021

Keywords:

Metal fuels
Particle microexplosion
Coalescence
Hybrid combustion
Iron carbonyl

ABSTRACT

This study investigated the combustion behaviors of pure iron and mixed particles, particularly iron–aluminum and iron–coal mixtures, doped into methane (CH₄)–air premixed flames. The mechanically mixed particles were prepared with a weight ratio of 1:1. Thermogravimetric analysis revealed that the Fe particles and the Fe–coal mixture underwent oxidation in similar regions of relatively low temperatures; the Fe–Al mixture underwent a multistage oxidation process. A conical CH₄–air premixed flame—with the CH₄–air equivalence ratio maintained at the stoichiometric value—was doped with micron-sized solid fuels at various feed rates. Increasing the particle feed rate appeared to alter the flame front characteristics. The interdependency between solid fuels and the CH₄–air premixed flame was investigated with respect to flame temperatures, gas emissions, and metal oxide products. Particle microexplosions occurred in the Fe–coal combustion. Regarding the mechanism underlying the microexplosions, we hypothesized that the bubbles inside the Fe particles may have contained dissolved O₂, N₂, and CO; the dissolved CO may have generated iron carbonyl (Fe(CO)₅). Coalescence, repeated bubbling, and bubble expansion processes led to the expansion of iron oxides with hollow shells. The rapid increase in inner pressure and explosive internal combustion caused by the ripening and flammability of the (Fe(CO)₅)/O₂ bubbles engendered the microexplosions. CO was added to the Fe flame to validate this hypothesis.

© 2021 The Combustion Institute. Published by Elsevier Inc. All rights reserved.

1. Introduction

Metals and metalloids, such as aluminum, iron, silicon, and magnesium, are the most abundant resources in the earth's crust [1]. Because of their high energy density and high chemical reactivity, which enhance combustion stability, metal particles are used in solid rocket propellants to increase the impulse density and propellant density [2–6]. Metals constitute appropriate propellant fuels for increasing propulsion output, which is critical in the industries of defense and space technology [7–9]. Moreover, metals are used in metal–water propellants and water-breathing propulsion systems for underwater vehicles [10], and they are comparable to hydrocarbon fuels as favorable potential energy carriers. Bergthorson [11] proposed a novel concept involving the use of recyclable metal fuels for clean zero-carbon power. Metal combustion can exhibit substantial exothermicity, and the generated exothermic energy can in turn be converted into power, heat, and electricity for diverse purposes; such combustion can

also yield solid metal oxides that, unlike carbon dioxide released from hydrocarbon flames, can be captured and recycled. However, advances in the application of metal hybrid combustion are complicated by the complexity of the process.

In general, metal particle combustion can be classified into three modes on the basis of the underlying characteristics and oxidation reaction of metals in hydrocarbon flames: modes A, B, and C [11,12]. In mode A, metals such as Al and Mg can undergo vapor-phase droplet combustion; the metal vapor may then react with the oxidizer to release heat. In mode B, metals such as boron and silicon undergo heterogeneous combustion but produce a gaseous oxide and suboxide. The gaseous suboxide reacts with an oxidizer, but a microflame occurs on the metal particle surface. In mode C, metals exhibit a notable phenomenon: they may react heterogeneously and produce metal oxides that coat the particles and increase their size. The ratio of flame temperature (T_f) to boiling temperature (T_b) can determine whether the metal burns homogeneously or heterogeneously. Specifically, a T_f/T_b ratio of >1 indicates homogeneous combustion (mode A), whereas a T_f/T_b ratio of <1 indicates heterogeneous combustion (mode B or C) [12]. Furthermore, the combustion mode is associated with the

* Corresponding author.

E-mail address: yueheng@mail.ncku.edu.tw (Y.-H. Li).

solid product particle size. Mode A and B fuels produce nanoscale oxides, whereas mode C fuel produces microscale oxides.

Of the solid metal fuels capable of producing larger solid combustion products, Fe is considered the best candidate for recyclable fuels. Fe has a high energy density, completely burns out during heterogeneous combustion, and yields larger metal oxide particles than do fossil fuels. In addition, Fe absorbs heat that is later released because of the heterogeneous reaction of the solid particles [13]. Regarding the combustion characteristics of Fe particles, Sun et al. [14] investigated the combustion zone propagating through an Fe particle cloud and the process of Fe particle combustion. Tang et al. [15] explored the effects of Fe particle size and the addition of diluent gas on the combustion modes of Fe particles. Concerning the combustion of metal composites, Chintersingh et al. [16,17] speculated that Fe had a catalytic effect on the heterogeneous oxidation of burning boron particles, which led to a reduction in the burning time. Hashim et al. [18] reported that the addition of Fe particles (approximately 1 wt% of the total sample mass) to solid fuels that were based on boron-/hydroxyl-terminated polybutadiene increased the burning rate.

Regarding the synergetic combustion behavior of metal particles, the vigorous reduction–oxidation reaction between a metal fuel and a metal oxide is a quintessential example. The thermite reaction of ferric oxide (Fe_2O_3) and Al has been extensively discussed [19], and the propagation rate of this reaction is associated with the equivalence ratio [20,21], architecture [22], and particle size of the reaction components [23]. Furthermore, metal particle microexplosions in hybrid flames could be attributed to synergistic combustion behaviors. Microexplosions have been noted in studies on the combustion of Al–Zr wire alloys [24], single-particle combustion of Al–Mg alloys [25], and combustion of Ti, B, Zr, and other elements [26–28]. Wainwright et al. [29] used phase-contrast X-ray imaging and a high-speed camera to observe internal bubbling and microexplosions during the wire combustion of ball-milled Al–Zr composite powder under various oxidation conditions. The Al vapor flame heated the particles while N_2 continued to act upon and dissolve into the particles, generating a molten Al–Zr–N solution that contained some oxygen. The researchers concluded that rapid bubbling triggered microexplosions in the composite powder and that slow bubbling in some particles resulted in the formation of spherical metal oxide particles.

In the present study, we examined Fe combustion because of the abundance of Fe ore deposits. To examine the interaction between two metal particles during combustion under different combustion modes, we added Al powder to the flames; Al powder was selected because of the high chemical reactivity of Al microparticles. To avoid the problem of carbon abatement encountered in conventional coal-fired power plants, we replaced pulverized coal with Fe powder. The combustion product of Fe could be readily captured and recycled. Consequently, carbon dioxide emission could be reduced.

2. Experimental methods

2.1. Material preparation and characterization

Particle size is a crucial parameter in the selection of solid fuels as energy carriers. Bergthorson et al. [12] specified that smaller particles have higher reaction rates because of their higher surface-area-to-volume ratios. Metal particles with diameters of $<20\ \mu\text{m}$ have burning velocities similar to those of hydrocarbon fuels. In the present study, particle size was examined using a particle sizer (Nanobrook 90Plus PALS, Brookhaven Instruments, USA), and the shape and surface characteristics of the particles were examined using scanning electron microscopy (SEM)–energy-dispersive X-ray spectroscopy (SEM-EDS; JSM-7000F, JEOL, Tokyo, Japan). Three

Table 1
Chemical composition of Fe, Al, and coal particles.

Material	Category	Shape	Composition analysis	
			Chemical composition	Concentration (%)
Fe	Fine Powder	Irregular cluster	Fe	98.86
			Mn	0.30
			P	0.03
			S	0.01
			C	0.01
			Si	0.02
Al	Fine Powder	Spherical bead	Al	98.00
			Cu	0.02
			Fe	0.20
			Si	0.20
			H_2O	0.10
Coal	Fine Powder	Irregular flake	C	88.92
			H	4.17
			O	5.25
			N	1.14
			S	0.52

Table 2
Particle size.

Material	D10 [μm]	D50 [μm]	D90 [μm]	Mean size [μm]
Fe	1.183	2.712	6.216	2.548
Fe–coal	1.262	1.755	2.440	1.876
Fe–Al	1.082	1.176	2.319	1.393

samples of solid fuels were provided by Sichuan Zichuan New Materials Technology Co., Ltd. (Chengdu, Sichuan, China): pure Fe, mechanically mixed Fe–Al, and mechanically mixed Fe–coal. Table 1 presents information on the morphology and chemical composition of the Fe, Al, and coal particles, as provided by the supplier (Zhangqiu Metallic Pigment Co. Ltd.). The Fe and Al particles were of 98.86% and 98.00% purity, respectively. The elemental composition of the pulverized coal was as follows: 88.2% carbon, 5.25% oxygen, 4.17% hydrogen, 1.14% nitrogen, and 0.52% sulfur. Notably, the Al particles contained 0.1% H_2O . Moreover, the Al particles were coated by an amorphous hydrophilic alumina shell (the thickness $\sim 3 - 5\ \text{nm}$) capable of absorbing a small amount of water from the atmosphere and containing oxygen. The mechanically mixed particles were prepared at a 1:1 wt ratio. Although the particles exhibited a heterogeneous size distribution, their diameters were $<5\ \mu\text{m}$. Furthermore, metal fuels with diameters of $<3\ \mu\text{m}$ (Table 2)—consistent with Bergthorson’s requirements for burning metal fuels in hydrocarbon flames [12,30]—were used for the comparison of combustion stability and flame characteristics. SEM-EDS (JSM-7000F, JEOL) was also conducted to determine the physical properties of the particles, including their shapes and surface characteristics. The SEM images of the particles before combustion are depicted in Fig. 1. Overall, the larger surface-area-to-volume ratios of the small particles affected the reaction and burning rates.

2.2. Burner and feeding system

The burner is a stainless steel coaxial nozzle (Fig. 2(a)) with an inner diameter of 11.5 mm, an outer diameter of 14.0 mm, and the overall length of 120 mm. The inner tube of this nozzle is a concentric reducer, which can help laminarize mixtures before their exit from the nozzle.

The feeding system was a low-concentration aerosol generator (RBG 1000 Palas GmbH, Germany), as illustrated in Fig. 2(b). The system is based on the principle of the rotating brush generator, which agitates dry, noncohesive dust particles into an airborne state. A pivoted brush with a cylindrical dorm located inside the

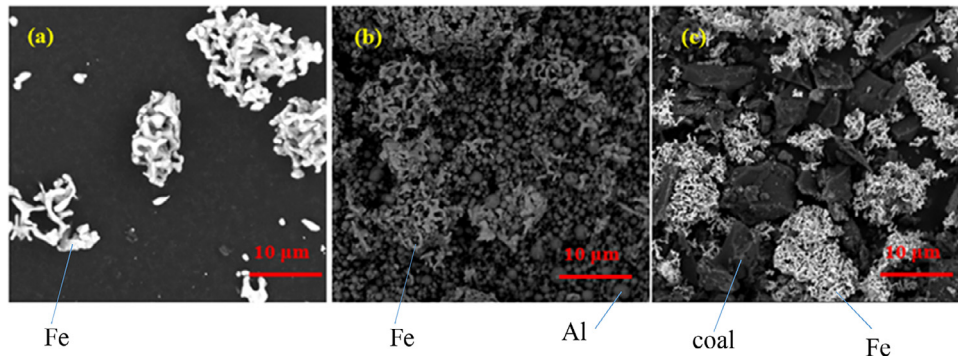


Fig. 1. Scanning electron microscopy images of (a) pure Fe, (b) mechanically mixed Fe–Al, and (c) mechanically mixed Fe–coal.

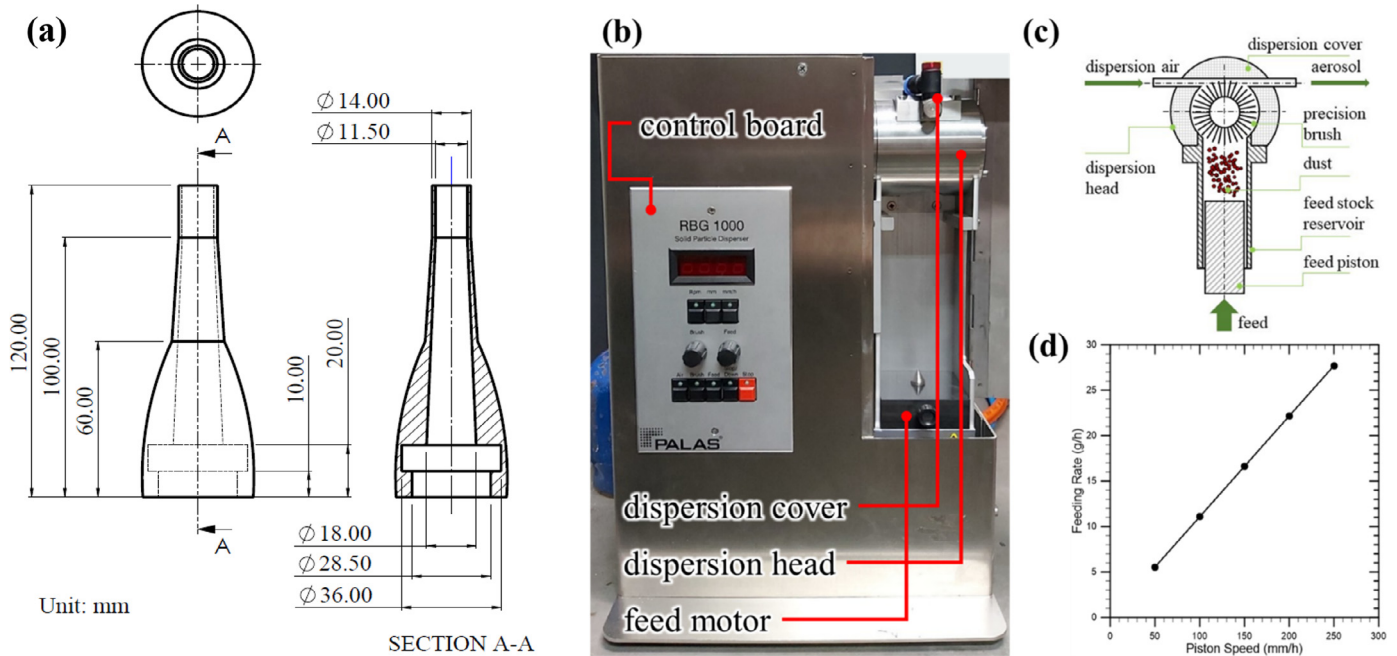


Fig. 2. (a) Stainless steel nozzle of the laboratory-scale metal burner, (b) photograph of the aerosol generator, (c) schematic of the aerosol feeding system, and (d) plot of particle feed rate against piston speed.

stainless steel tube blocks the dispersion head (Fig. 2(c)). A powder reservoir is located below the cylindrical brush. The piston pushes the compacted powder at a constant speed set using the electronic panel, and the rotating brush carries and delivers the powder to the dispersion head. Figure 2(d) displays a plot of the feed rate of this powder dispersion and the piston speed. The powder is mixed with the carrier gas and delivered into the combustion chamber. The feed rate and mass concentration can be digitally controlled by setting the piston velocity. The mass flow or the solid particle feed rate indicates the quantity of dust injected with the carrier gas per unit time.

2.3. Experimental setup

Figure 3 illustrates the setup for the laboratory-scale experiment on the combustion of metal particles in methane (CH₄)–air flames. The aerosol generator was used to deliver the metal particles to the inner nozzle of the coaxial burner, and the metal particle feed rate was controlled by adjusting the piston speed on the aerosol control panel. The carrier gas was mixed with the metal particles in advance and transported to the T junction for incorporation with the delivered CH₄ before exiting the combustion nozzle. In all cases, the CH₄–air equivalence ratio was

maintained at the stoichiometric value and calculated using the fuel and oxidizer ratios.

To analyze the solid product of the hybrid flames, we used square mesh nickel grids with a bar width of 6 µm and an open area of 58% (Nickel 1000mesh, PolySciences, USA), in addition to using stainless steel reverse action tweezers (P-651, Hozan, Osaka, Japan) with a tip width of 0.2 mm and a double-acting air actuator. To control the air exhaust and air pressure of the actuator, we managed the timing of piston movement by using a micro-controller board (Arduino Mega 2650) and a controllable solenoid valve. The piston was controlled to remain within the flame for 1 s to capture the solid products.

NO_x, CO₂, and CO emissions were monitored using the Vario Luxx Emission Analyzer (MRU Instruments, USA) with a cotton-packed filter connected at the suction port. The sampling pipe was placed 120 mm above the burner nozzle, and the sampling rate of the analyzer was 1 Hz.

To examine the concentrations of particles added to each hybrid flame, a photograph was captured using a digital single-lens reflex camera (D80, Nikon, Japan) attached to a large-aperture lens (30 mm; F1.4 EX DC HSM, SIGMA, USA). The camera settings (ISO 100, shutter speed 1/25 s, f 5.6) were constant. Moreover, a high-speed camera (MEMRECAM ACS-3, NAC, Japan) with a macro

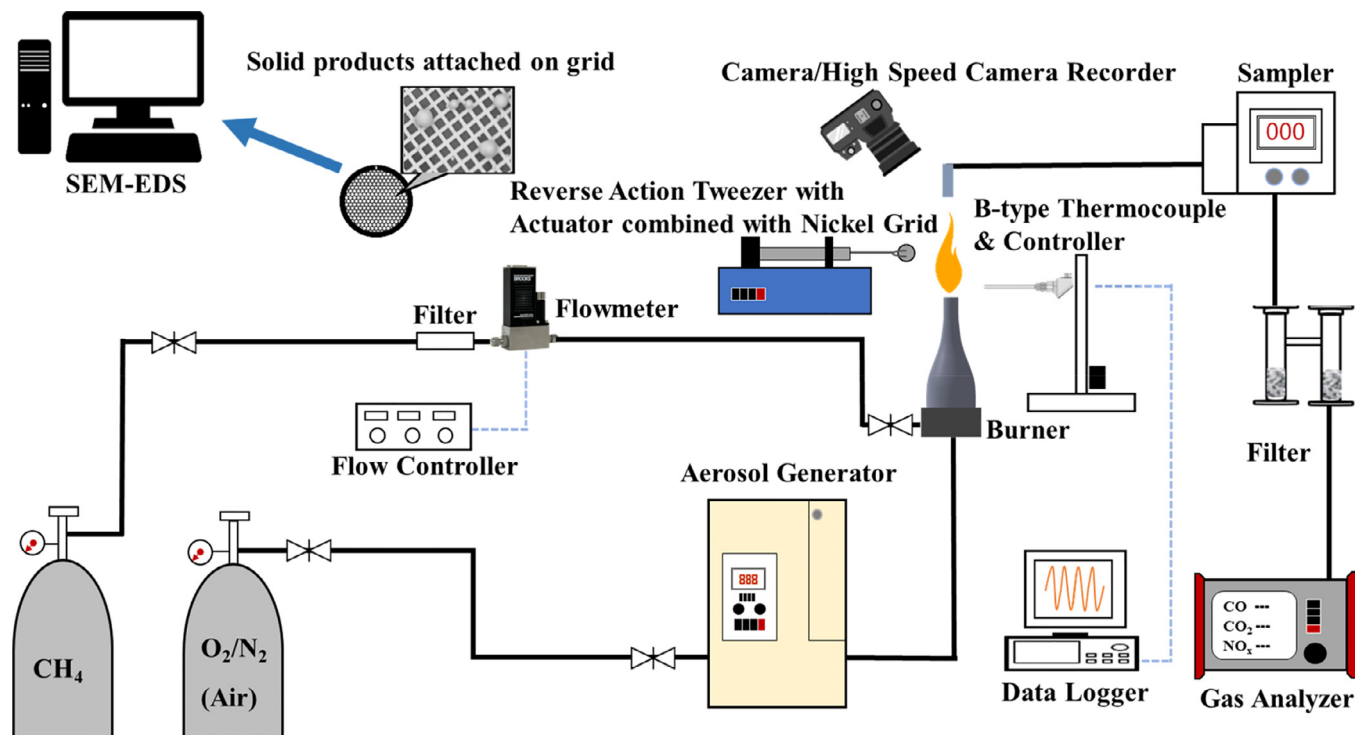


Fig. 3. Experimental setup and measurement system.

lens (MACRO 105-mm F2.8 EX DG OS HSM, SIGMA, USA), a frame rate of 20,000 fps, and a shutter speed of $49.5 \mu\text{s}$ was used to determine the flying trajectory and burning characteristic of metal particles in the hybrid flame.

The flame temperature profile along the central line of each hybrid premixed flame was determined using a B-type thermocouple with a maximum temperature of approximately 2000 K. The thermocouple signals were logged and converted to temperature data by using a data logger (NI-USB-TC01, National Instruments Corp., USA). The vertical position of the thermocouple was precisely controlled by a linear motion system (PAB-S4S3R015, EZ Limo, Japan), and the thermocouple traversed between 0 and 120 mm above the burner exit with a step interval of 5 mm.

3. Results and discussion

3.1. Metal combustion

3.1.1. Thermogravimetric analysis

A thermogravimetric analyzer (TA-SDT 2960, TA Instrument, USA) was used to examine the thermal stability of the mixed solid fuels. Approximately 8 mg of metal fuels with particle diameters of $<10 \mu\text{m}$ was placed in a crucible bowl. Each fuel was heated at 303 K for 5 min and then heated up to 1125 K. The heating and air flow rates were 10 K/min and 100 mL/min, respectively. The temperature and weight variation trends observed in this study could be divided into three regions: a preheat zone (from 300 K to the ignition temperature of solid particles, T_{ignition}), metal oxidation zone (from T_{ignition} to the oxidation temperature of solid particle combustion, $T_{\text{oxidation}}$), and metal oxide production zone (from $T_{\text{oxidation}}$ to 1125 K). The ignition temperature was determined through the intersection method [31,32]. For each metal particle, the oxidation temperature was defined as the temperature at which the fuel reached the maximum mass gain, similar to the theoretical gain. For example, the oxidation temperature for Fe

was the temperature at which the metal was oxidized to become Fe_2O_3 with a theoretical mass gain of 43%.

Figure 4 illustrates thermogravimetric and derivative thermogravimetric curves demonstrating the weight variation and thermal behaviors of Fe, Al, and coal with increasing temperature as well as the peak temperature in various oxidation stages. Figure 4(a) demonstrates the results observed in the single-step oxidation process of pure Fe, in which 848 K was the peak temperature. The Fe particle weight increased significantly with temperature. When the temperature reached 994 K, the weight gain of iron oxide decreased. According to some studies [33,34], Fe is oxidized through the formation of an intermediate product through the following process: $\text{Fe} \rightarrow \text{FeO} \rightarrow \text{Fe}_3\text{O}_4 \rightarrow \text{Fe}_2\text{O}_3$. Notably, the mass gain percentage of Fe also corresponded with the theoretical value of 43%. Figure 4(b) presents the results observed in Al oxidation process at a fixed heating rate of 10 K/min. The preheat zone of the Al particles involved higher temperatures than did those of the Fe or coal particles. The preheat zone started at 800 K, and the ignition temperature was approximately 824 K. Multiple oxidation stages were noted for the Al particles. In general, the oxidation process of Al particles can be divided into four stages [35]. In the first stage, when the temperature is <550 K, the aluminum oxidation rate is slow. In the second stage, the temperature is between 550 and 650 K. In the present study, the mass did not increase during this stage. In the third stage, when the temperature is between 650 and 1000 K, the aluminum oxidation rate increases continuously, as indicated by the derivative gravimetric curves. According to Trunov et al. [36], in the fourth stage, when the temperature exceeds 1100 K, the maximum mass gain approaches 19%. In the X-ray diffraction performed in that study [36], no definitive patterns were observed in the first stage. In the second and third stages, the patterns indicated a transition from Al_2O_3 to $\gamma\text{-Al}_2\text{O}_3$ and from Al_2O_3 to $\theta\text{-Al}_2\text{O}_3$, respectively. Because the maximum temperature in the present study was only 1125 K, the fourth stage is considered herein. The pattern indicates a transition from $\gamma\text{-Al}_2\text{O}_3$ to $\alpha\text{-Al}_2\text{O}_3$ during this stage. Figure 4(c)

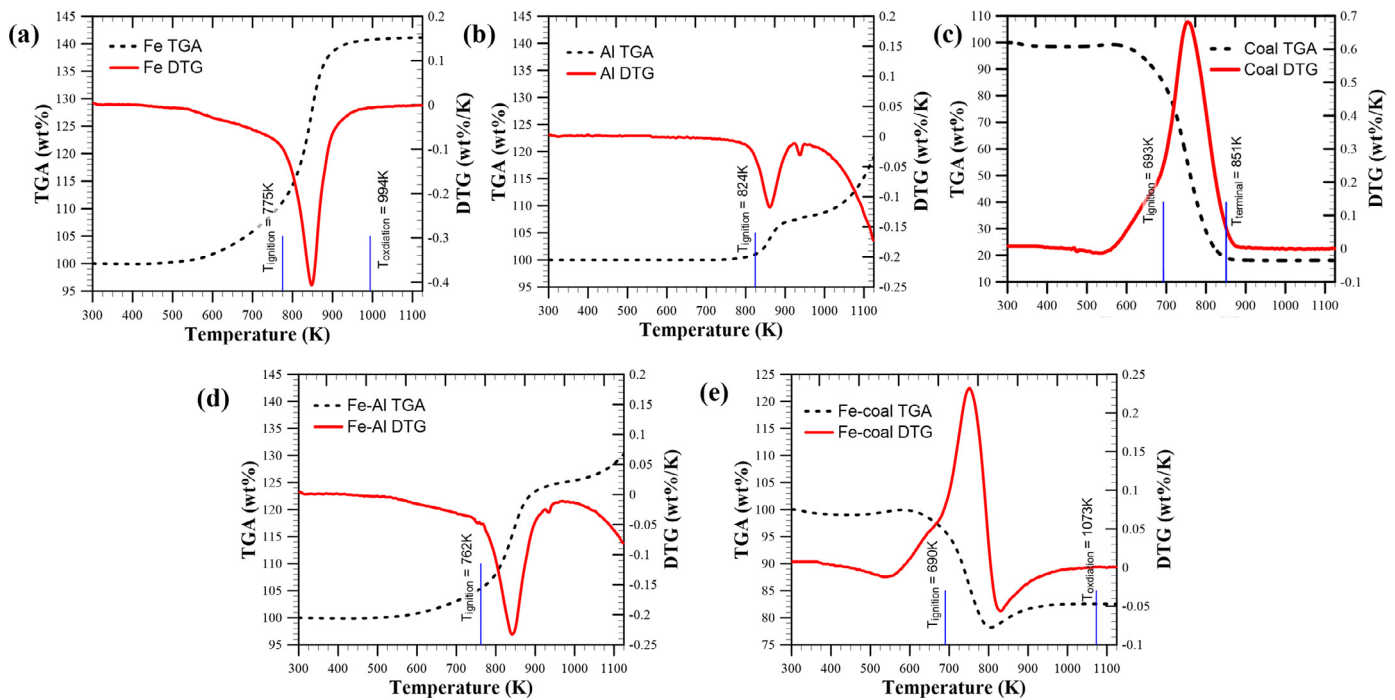


Fig. 4. Thermogravimetric and derivative thermogravimetric curves for (a) Fe, (b) Al, (c) coal, (d) mechanically mixed Fe–Al, and (e) mechanically mixed Fe–coal.

displays the results observed in the oxidation of the coal particles at 300–1125 K and at ignition temperatures of 693 K. The terminal temperature (T_{terminal}) of coal particle was defined as the temperature at which the fuel conversion reaches 99% [31,32]. The formula of fuel conversion is expressed as $[(W_i - W)/(W_i - W_f)] \times 100\%$, where W_i and W_f are the initial and final weight of fuel, respectively. The coal oxidation process was completed when the temperature reached 851 K, with the particle weight decreasing by approximately 80% relative to the initial weight. In contrast to that of Fe, the oxide product of coal may eventually be converted into gaseous oxides such as carbon dioxide and carbon monoxide.

The mechanically mixed Fe–Al particles were oxidized through multiple stages (Fig. 4(d)). Fe–Al oxidation stage divided into two stages according to the oxidation for Fe and Al particle. When the temperature reached 553 K, Fe commenced to oxidize in the first stage and convert to Fe_2O_3 [33]. When the temperature reached 890 K, the second stage oxidation began; that is, Al particle started to oxidize and convert to $\alpha\text{-Al}_2\text{O}_3$ [37]. Mass gain for Fe–Al case (30% mass gained) is lower than that for pure Fe case (43% mass gained) but higher than the pure Al case (19% mass gained).

Figure 4(e) shows the thermogravimetric and derivative thermogravimetric curves of the Fe–coal oxidation. Simultaneous oxidation and weight loss occurred within a range of low temperatures. Rapid weight loss occurred between 570 and 800 K, indicating that the carbon was completely oxidized and entered a stage of transition from solid to gas. Furthermore, Fe was not completely oxidized. The curves suggest that the Fe–coal oxidation process was similar to the coal oxidation process in that it occurred within a range of relatively low temperatures. The Fe–coal oxidation process was complete even before the temperature reached 1100 K. At the end of the oxidation process, the weight loss recorded when the sample had been thoroughly oxidized was approximately 17% of the initial weight, and the maximum derivative thermogravimetric peak was recorded at 750 K.

3.1.2. Observation of single-fuel combustion

Photographs of the single-fuel premixed flames (i.e., pure CH_4 , Fe– CH_4 , Al– CH_4 , and coal– CH_4 flames) are depicted in Figure 5.

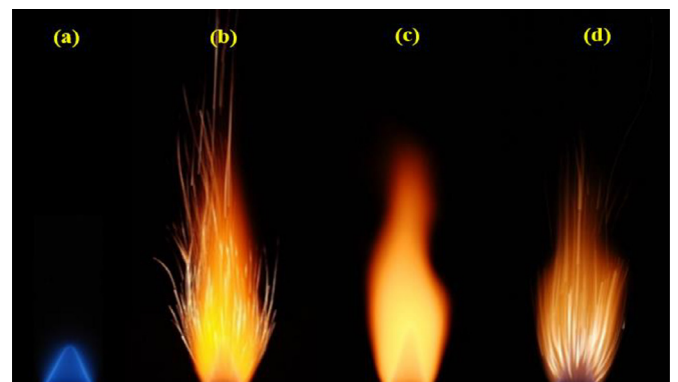


Fig. 5. Hybrid combustion of single fuels at a piston speed of 46.48 g/m³: (a) CH_4 , (b) Fe, (c) Al, and (d) coal.

Although the feed rate was maintained at 46.48 g/m³, the injection of different particles may have affected the coupled flame front characteristics of the hybrid premixed flames. Injecting higher concentrations of particles led to changes in the flame cone size and flame color. The outline of the CH_4 flame front is presented in Fig. 5(a); a comparison of the CH_4 and Fe flame fronts revealed that the speed of the Fe flame (Fig. 5(b)) was comparable to that of the CH_4 flame, enabling the formation of a coupled flame front. The Al combustion process produced a bright and distinct flame cone (Fig. 5(c)). In contrast to the observation made for the hybrid Fe– CH_4 flame, we did not observe particles in the post combustion zone. This is attributable to the homogeneous reaction during Al/ CH_4 combustion, which produced Al vapor and solid nano-oxides. The brightness of the flame cone indicates that the Al vapor mixtures reacted with the premixed CH_4 and air in the flame reaction zone. By contrast, the hybrid coal– CH_4 combustion process formed a blue CH_4 flame rather than a coupled flame front (Fig. 5(d)). Coal particles were mostly ignited after they passed the flame sheet. Julien et al. [13] suggested that two flames should have similar levels of heat release so that the flame speeds can

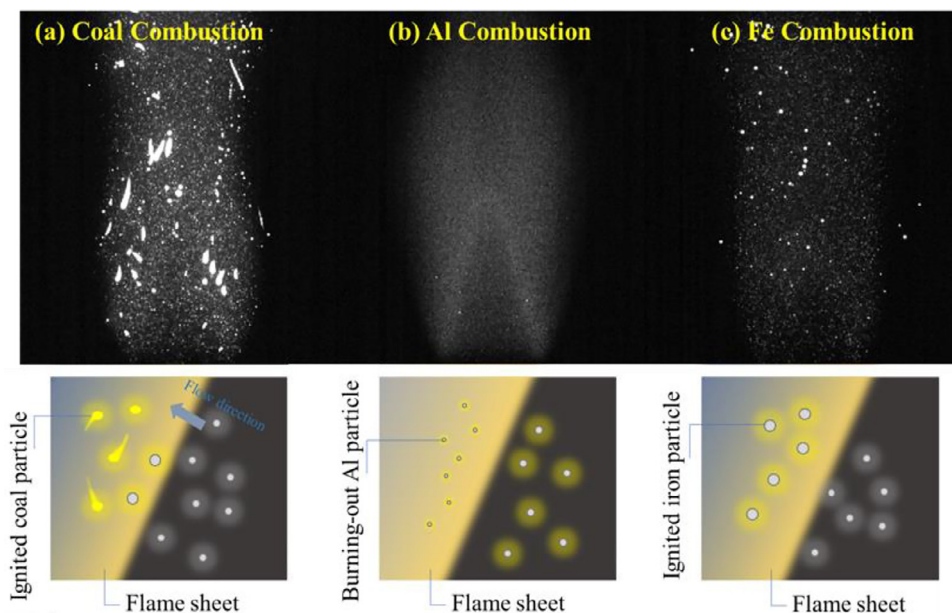


Fig. 6. Particle morphology photographs of premixed CH₄-air flame doped with (a) coal particles, (b) Al particles, and (c) Fe particles.

be matched, thereby facilitating the formation of a coupled flame front. However, in the present study, a coupled flame front was not observed under these conditions, meaning that the heat release of the coal particles was insufficient and was not comparable to that of the CH₄ flame products.

Figure 6 depicts photographs captured using a high-speed camera for the observation of particle combustion. Regarding the hybrid coal-CH₄ flame (Fig. 6(a)), flying coal particles that penetrated the flame front were mostly ignited, producing comet-tail-like traces. As presented in Fig. 6(b), the particle outlines were barely visible within the hybrid Al-CH₄ flame cone because of the evaporation of Al, and they almost disappeared in the post flame region. By contrast, as illustrated in Fig. 6(c), Fe particles within the hybrid Fe-CH₄ flame cone manifested as dim dots and began to glitter after flying through the flame front. During the ignition stage of Fe, the outer particle surfaces were oxidized by hot gas, producing small, thin-shelled agglomerates of Fe oxide. After the metal passed through the flame front, the diffusion regime was dominant, inducing the combustion product to diffuse to the thin shell.

3.1.3. Observation of mixed-fuel combustion

The effects of various particle feed rates (9.30, 18.59, 27.89, 37.19, and 46.48 g/m³) on the hybrid premixed flames were examined. As shown in Fig. 7, Fe particles were injected into the CH₄-air premixed flame at different concentrations. Injecting 9.30 g/m³ of Fe particles into the CH₄-air premixed flame resulted in the appearance of a blue flame cone (Fig. 7(a)). The Fe particles ignited and oxidized in the hot environment; the trajectories of the burning particles were observable. When the particle concentration was raised to 18.59 g/m³ at a piston speed of 100 mm/h, the heat released by the Fe particles was sufficient to form a flame front. Under this circumstance, the flame cone became thicker, and the thin blue CH₄ flame cone and the thick yellow Fe flame cone were coupled (Fig. 7(b)). However, in general, this double-front flame cone structure occurs only above a certain critical concentration, which coincides with the point at which the Fe flame front is formed [13]. Accordingly, as displayed in Fig. 7(c)–7(e), when the feed rate was further increased (up to 46.48 g/m³), the flames grew brighter and more stable. Figure 7(f)–(j) depicts the Fe-Al premixed flames; coupled flame cones were observed at all feed rates.

Depending on the particle concentration, the flame intensity appeared stronger, especially on the hybrid flame front. When the Fe-coal feed rates were 9.30 to 27.89 g/m³ (equivalent to 50 to 150 mm/h), a blue flame originating from the CH₄-air premixed flames was observed (Fig. 7(k)–7(m)). When the feed rate was 37.19 g/m³ (equivalent to 200 mm/h), a coupled flame front was observed. This phenomenon demonstrates the importance of particle concentration in the formation of coupled flame fronts, which vary depending on the combustion regimes between gas and solid fuels in stabilized hybrid flames. Notably, only the flames doped with Fe-coal caused particle microexplosions; the burned particles exhibited a zigzagging and branching trajectory. The microexplosions are detailed in Section 3.5.

3.2. Temperature measurement

In the temperature measurements, the feed rate was maintained at 27.89 g/m³ to ensure that all the metal-doped CH₄ flames featured a coupled flame front. As shown in Fig. 8(a), the temperature profiles of the undoped and Fe-doped CH₄ flames were similar, although they exhibited subtle differences in the downstream regions. The temperature for the doped flame was slightly higher than that for the undoped flame, with the maximum temperature variation being 40 K. Regarding the Fe-doped CH₄ flame, the temperature rose rapidly, peaking at approximately 1873 K near the flame cone tip. It then declined continuously in the downstream and reached 1087 K at 120 mm. The effects of various feed rates on temperature were also investigated (Fig. 8b). As mentioned, the Fe-doped CH₄ flame was roughly similar in temperature to the undoped CH₄ flame. The Al-doped CH₄ flame was higher in intensity than the Fe-doped CH₄ flame, and the addition of coal moderated this intensity. The peak temperatures of the Al-, coal-, and Fe-doped flames occurred near the flame cone tip at 2000, 1800, and 1873 K, respectively. Nevertheless, in all three cases, the temperatures in the upstream zone (0–10 mm) and the downstream zone (95–120 mm) were relatively similar. We also studied the effects of the addition of two fuel blends (Fig. 8(c)): Fe-Al and Fe-coal (50:50 for both). The overall temperatures of the Fe-Al-doped and the Fe-coal-doped CH₄ flames were still higher and lower than that of the pure Fe-doped CH₄ flame, respectively. The addition

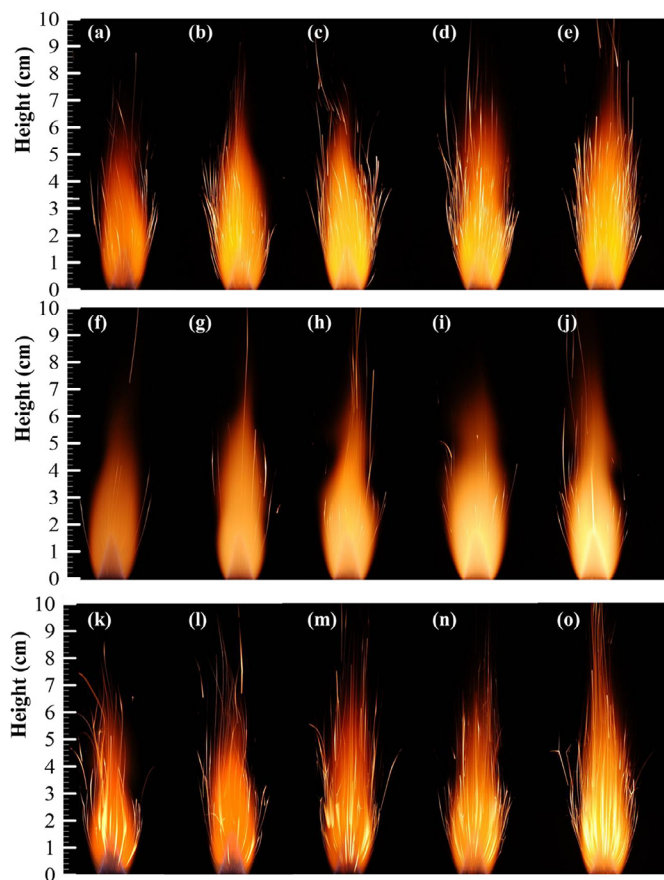


Fig. 7. Photographs of premixed flames of (a–e) pure Fe, (f–j) mechanically mixed Fe–Al, and (k–o) mechanically mixed Fe–coal at various feed rates: (a, f, k) 9.30 g/m³; (b, g, l) 18.59 g/m³; (c, h, m) 27.89 g/m³; (d, i, n) 37.19 g/m³; and (e, j, o) 46.48 g/m³.

of coal to the Fe-doped flame lowered the peak temperature to 1698 K, which can be explained by the lower energy density and specific energy of the coal particles. We speculated that the CO emitted in coal combustion reacted with the Fe particles to form iron carbonyl (Fe(CO)₅), a flame inhibitor, thus reducing the temperature. Furthermore, the addition of Al to the Fe-doped flame increased the peak temperature to 1967 K; this can be attributed to not only the Al particles' high energy density but also the exothermicity of the homogeneous Al vapor reaction. The addition of coal

Table 3
Gas emissions of Fe, Fe–Al, and Fe–coal in hybrid CH₄–air premixed combustion.

Materials	Gas emission			
	O ₂ (%)	CO ₂ (%)	NO _x (ppm @ 3%O ₂)	CO (ppm @ 3%O ₂)
Fe	14.1	5.3	224	32
Al	12.19	5.8	200	33.61
Coal	13.26	5.07	170	25.55
Fe–coal	13.9	7.4	176	278
Fe–Al	14.9	5.2	257	34

and Al to the Fe-doped flame changed the position of the tip of the flame cone.

3.3. Gas emissions

Table 3 presents a comparison of the flue gas emissions from the various combustion processes. Carbon emissions, including those of CO and CO₂, constituted the primary product of the hydrocarbon flames. The measured CO and CO₂ concentrations were similar for the Fe, Al, and Fe–Al combustion processes because the combustion of metal fuels does not increase the emission of carbon gases, only the combustion products. However, the NO_x concentrations in the Fe and Fe–Al flames were high. Metal particles and CH₄ fuel contain no nitrogenous compounds; apart from fuel NO, NO_x primarily originates from thermal NO and prompt NO. Thermal NO_x, which is highly temperature dependent, was formed through the simple heating of oxygen and nitrogen in a flame. Prompt NO_x formed rapidly from the interaction of nitrogen and oxygen with some of the active hydrocarbon species derived from the fuel in the hydrocarbon flames. Constitutive reactions involving thermal NO_x and prompt NO_x are associated with oxidizing radicals (O, H, and OH) [38]. In the present study, the NO_x emission concentrations at 3% O₂ for Fe and Fe–Al were 224 and 257 ppm, respectively. Notably, the Fe–coal combustion process was associated with the highest increase in CO emission; this is ascribable to the fact that most of the coal particles were devolatilized once they passed through the flame cone and ignited, producing a large amount of CO and CO₂. The CO and CO₂ concentrations in the Fe–coal combustion process were 278 ppm and 7.4%, respectively; those in the Fe combustion process were 32 ppm and 5.3%, respectively; and those in the Fe–Al combustion process were 34 ppm and 5.2%, respectively. In addition, the NO_x concentration in the Fe–coal combustion process was approximately 176 ppm, which was the lowest among the three processes. The temperature of the Fe–coal premixed flame was sufficiently low to reduce the contribution of thermal NO_x. In general, the presence of Fe(CO)₅ in

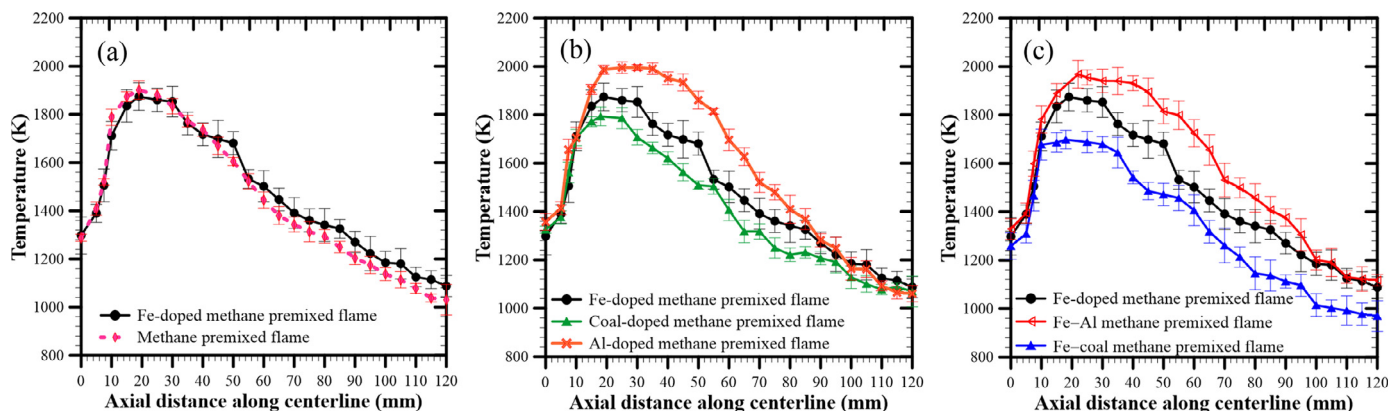


Fig. 8. Measured temperature distribution along the center line of (a) undoped and Fe-doped premixed CH₄ flames; (b) the Fe-, coal-, and Al-doped premixed CH₄ flames; and (c) the Fe-, Fe/Al-, and Fe/coal-doped premixed CH₄ flames.

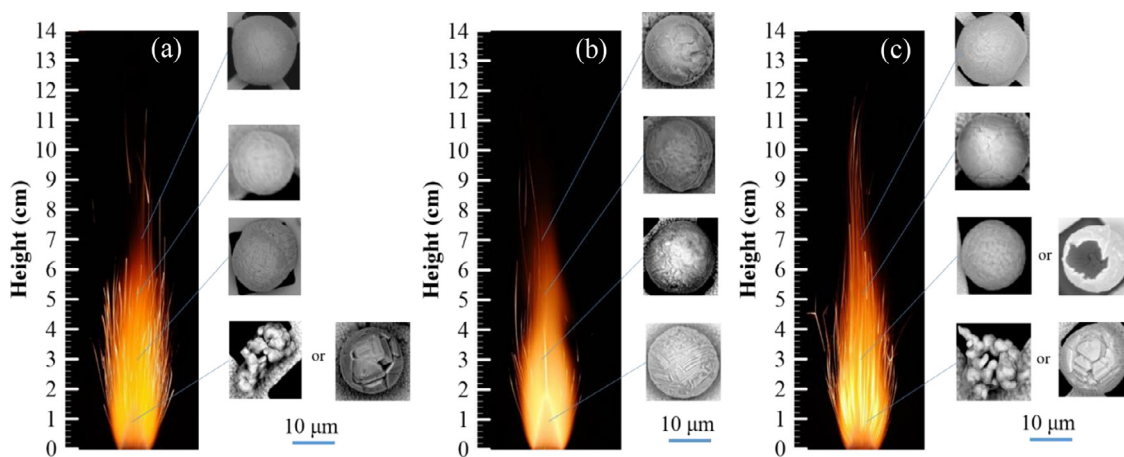


Fig. 9. Transformation of iron oxide particles at various positions in the CH_4 -air premixed flames: (a) Fe, (b) Fe-Al, and (c) Fe-coal.

flames induces radical scavenging [39]. Reducing oxidizing radicals leads to the simultaneous drop in the reactivity of thermal NO_x and prompt NO.

3.4. Combustion product analysis

3.4.1. Morphological observations before and after the reaction zone

We investigated the transformation of the oxide particles by placing sampling particles at four designated positions (DPs) above the burner: 10, 30, 50, and 70 mm. The particles were collected using a grid clipped with reverse action tweezers with a 0.2-mm tip, and their surface geometries and atomic concentrations were analyzed through SEM-EDS. Figure 9 illustrates the evolution of the particles' shape deformation at the DPs in the Fe, Fe-Al, and Fe-coal (CH_4 -air) flames. In the Fe and Fe-coal flames, some particles captured at the DP of 10 mm (within the flame cone) exhibited an irregular shape. Because the DPs of 10 mm were located in the upstream region of the reaction zone, not all the particles were subjected to temperatures sufficiently high to cause fusion and deformation. This explains why other particles were smoother or even spherical. Once the particles passed through the reaction zone, they transformed completely into spherical iron oxides. In contrast to the two other flames, the Fe-Al hybrid flame (Fig. 9(b)) released a sufficient amount of heat to cause deformations in all the particles, even at the DP of 70 mm. The particles collected from all four DPs were spherical, which is attributable to the higher temperatures within the flame cone. Brighter flame intensities under Al combustion may increase the thermal radiation capability of solid particles as well as the probability of transformation and the rate of expansion of solid irregular Fe particles, regardless of whether the particles are in the preheat or reaction zone. The probability of $\text{Fe}_2\text{O}_3/\text{Al}$ (a type of thermite) formation in Fe-Al hybrid flames is extremely small because Al is prone to ignite and react with oxygen prior to Fe oxidation. Regarding some studies relevant to the kinetic oxidation of pure Fe and pure Al cases [34,40,41], the products of Fe and Al oxidation are Fe_2O_3 and $\alpha\text{-Al}_2\text{O}_3$, respectively, when the flame temperature of a Fe-Al hybrid flame is around 1100–2000 K, as shown in Fig. 8c. In addition, the TGA result indicated the product of iron oxide is prone to Fe_2O_3 when the temperature is higher than 1100 K [33,34]. Therefore, there is barely pure Al existing in flame, whereas Fe_2O_3 may primarily exist in flames. It leads to an infinitesimally-lower probability of thermite formation in Fe-Al hybrid flames.

Cracked oxide particles, observed only in the Fe-coal hybrid flame, were primarily located in the post combustion region

(Fig. 9(c)). The particles in this region—specifically, small, thin-shelled agglomerates of iron oxide particles—may have been oxide particles that had already exploded because of the high-pressure gas bubbles trapped within them.

3.4.2. Analysis of Fe and O concentrations in particulate products

The combustion products of Al and coal were either gaseous (Al_2O_2 , AlO , Al_2O , and AlO_2 from the Al flames; CO and CO_2 from the coal flames) or nanoscale solids (e.g., Al_2O_3 from the Al flames). This indicates that the combustion products collected from the mesh nickel grids comprised only iron oxides.

Figure 10 illustrates plots of the Fe and O concentrations against the DPs for the Fe, Fe-Al, and Fe-coal flames. The atomic oxygen concentrations, which were initially low, increased as the DP increased. Regarding the Fe concentration, an inverse pattern was observed—that is, it decreased as the DP increased. At the DP of 10 mm, the O concentrations in the Fe, Fe-Al, and Fe-coal flames were 12%, 8%, and 11%, respectively. At the DP of 70 mm, the concentrations rose to 25%, 23%, and 25%, respectively. A possible reason for the lower O concentration observed at the DP of 10 mm for the Al-Fe flame was that the rate of the homogeneous Al oxidation reaction was faster than that of the heterogeneous Fe oxidation reaction. Despite the slight differences in the O and Fe concentrations between the three flames, the O-Fe ratios were all in the range of 19% to 22% when the DP was ≥ 30 mm. According to the phase diagram of Fe oxidation constructed by Darken and Gurry [42], the temperature measurements and O-Fe ratios confirm that the Fe particles were oxidized after passing through the reaction zone (approximately at the DP of 10 mm) and that the iron oxides were related to $\text{FeO}_{(s)}$.

3.5. Microexplosions in Fe-coal hybrid combustion

In the hybrid CH_4 -air flames doped with coal and Fe particles, the primary, secondary, and tertiary explosions were accompanied by particle microexplosions. To determine the mechanism underlying the microexplosions, we used a high-speed camera to record the behavior of the burning particles at a fixed particle feed rate of 46.48 g/m^3 (equivalent to 250 mm/h).

Unlike the hybrid combustion of pure Fe, the hybrid combustion of Fe-coal significantly increased the CO concentration because of the combustion product of the coal particles. Thus, the CO concentration in the post combustion region increased substantially. CO may have diffused through the surface of the Fe particles and reacted with Fe to form $\text{Fe}(\text{CO})_5$, an explosive gas. The expansion of the gaseous bubbles of $\text{Fe}(\text{CO})_5$ inside these

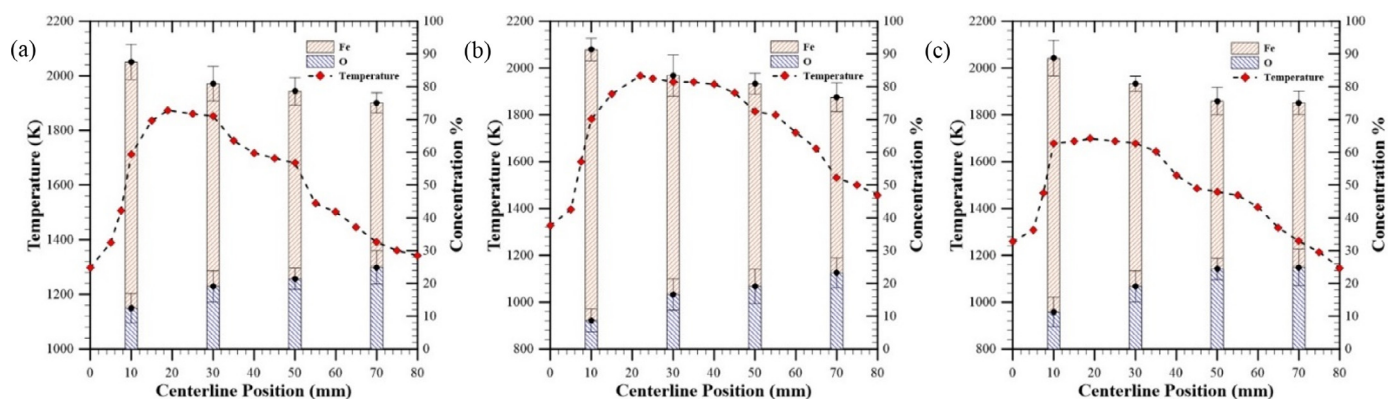


Fig. 10. Solid combustion products of Fe particles as a function of temperature and concentrations of (a) Fe, (b) Fe–Al mixtures, and (c) Fe–coal mixtures.

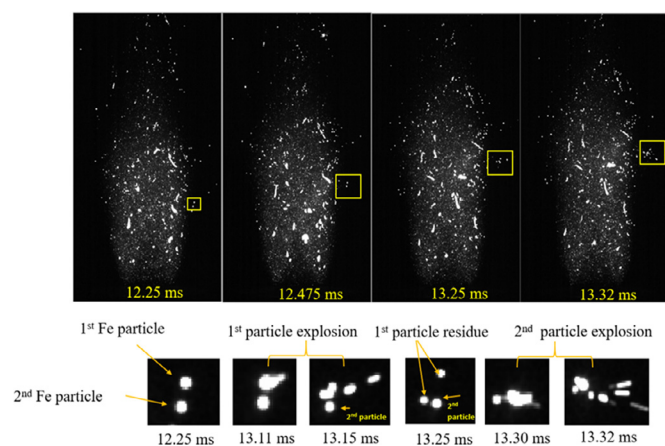


Fig. 11. Particle explosion in the Fe–coal hybrid flame triggering the explosion of a nearby particle. The particle feed rate was maintained at 46.48 g/m^3 (equivalent to 250 mm/h).

particles also led to an increase in surface tensile stress. Once the tensile stress exceeded the maximum bearing capacity of the particle surface, the particles exploded. Notably, the explosions in the Fe–coal hybrid flame may have triggered explosions in nearby particles (Fig. 11). The video clips of the Fe, Fe–Al, and Fe–coal hybrid (CH_4 –air) premixed flames are provided in Supplementary Information.

Figure 12 presents a schematic of the mechanism underlying particle microexplosions in the hybrid Fe–coal combustion process. The mechanism is summarized as follows: Once they reach the flame sheet, Fe particles are ignited, whereas coal particles are devolatilized, producing CO , H_2 , and CH_4 . The products of the coal combustion are extremely high emissions of CO and CO_2 , which occur downstream. During the oxidation process, Fe particles expand, become small agglomerates of Fe-oxide, and allow O_2 , N_2 , and CO to diffuse into the shell of the Fe particles and form bubbles within the particles. O_2 and N_2 may grow at an excessively slow rate, which could not trigger microexplosions; nevertheless, they undergo multiple steps of growth, including ripening, coalescence, and growth, that lead to the formation of thin-walled, hollow-shelled iron oxide products [29]. The repeated nucleation, growth, and bursting of bubbles within particles without particle fragmentation can result in spherical or cracked particles (Fig. 12). Nevertheless, CO bubbles may promote the heterogeneous formation of $\text{Fe}(\text{CO})_5$ across the inner surface of the particle shells, which constitutes the major cause of Fe particle microexplosion. The $\text{Fe}(\text{CO})_5$ bubbles may coalesce with O_2

Table 4

CO concentrations added to the combustion of Fe– CH_4 –air premixed flames.

Flow rate (L/m)			Vol%		
CO	CH_4	Air	CO	CH_4	Air
0.0093	0.613	5.8345	0.0014	0.0949	0.9036
0.0185	0.613	5.8345	0.0029	0.0948	0.9023
0.0278	0.613	5.8345	0.0043	0.0947	0.9010
0.0650	0.613	5.8345	0.0100	0.0941	0.8959
0.1298	0.613	5.8345	0.0197	0.0932	0.8871

bubbles. When a certain particle temperature is reached ($\text{Fe}(\text{CO})_5$ autoignition temperature: $\sim 323 \text{ K}$), the combustible $\text{Fe}(\text{CO})_5/\text{O}_2$ bubbles burst, completely fragmenting the particles.

3.6. Microexplosion in Fe-doped CH_4 flame with CO addition

A particle microexplosion occurred during the hybrid combustion of the Fe–coal premixed flame. It could have been caused by the increase in CO concentration due to thermal pyrolysis and the devolatilization of coal particles, which diffused to the small, thin-shelled agglomerates of Fe_2O_3 particles. The CO trapped inside the spherical Fe particles was prone to react with Fe and produce $\text{Fe}(\text{CO})_5$. However, $\text{Fe}(\text{CO})_5$ is flammable, with the corresponding explosive limit ranging between 3.7% and 12.5%. Accordingly, we hypothesized that the resulting CO was the precursor of the particle microexplosion. To verify this hypothesis, we considered five incremental concentrations of CO to be added to the Fe-doped hybrid flame (Table 4). Moreover, CO was added to the CH_4 –air premixed flame at the stoichiometric condition to simulate the high- CO environment in the hybrid combustion of the Fe–coal premixed flame. The incremental CO concentrations were added to the flame to understand the connection between the CO -derived $\text{Fe}(\text{CO})_5$ formation and the particle microexplosion.

Microexplosions were observed even at low CO concentrations (1.4×10^{-3} to 19.7×10^{-3} vol%), suggesting that CO may have triggered the microexplosions in Fe particles. We posited that the injection of higher CO concentrations (10^{-2} and 19.7×10^{-3} vol%) would not markedly increase the probability of microexplosions because of CO concentration saturation. The added CO is prone to bond chemically with heated Fe particles within the flame cone. The remaining CO may burn out while passing through the flame cone. Specifically, CO concentration saturation signifies that a maximum quantity of CO is required to react with heated Fe particles in the flame cone within a limited residence time. During the shape transition of the Fe particles from irregular to spherical, the chemically bonded CO would be wrapped inside the spherical

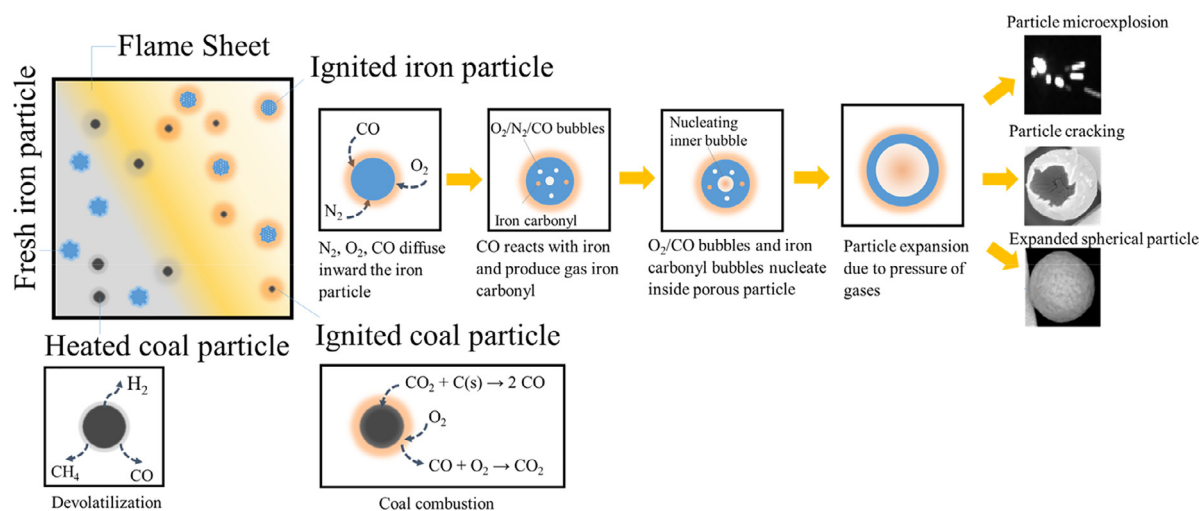


Fig. 12. Mechanism of particle microexplosions in hybrid combustion.

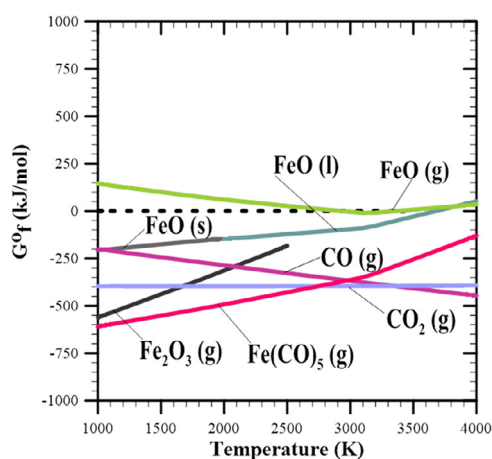


Fig. 13. Formation of Gibbs free energy and phase changes in possible Fe-coal combustion products, as derived from the NIST-JANAF thermochemical tables. Species with values of <0 kJ/mol will form spontaneously, whereas those with values of >0 kJ/mol will not form spontaneously.

particles, which may result in the chemical formation of $\text{Fe}(\text{CO})_5$ across the inner surface of the particles. The coexistence of $\text{Fe}(\text{CO})_5$ and CO would then trigger particle microexplosions. However, in general, CO exists only in the preheat zone but combusts in the flame sheet. Accordingly, CO concentration saturation is dependent on the maximum CO concentration—that is, the concentration at which the chemical bonding process with Fe within the flame cone can be completed.

According to the NIST-JANAF thermochemical tables [43], in air, only O_2 reacts with Fe. Figure 13 presents the Gibbs free energy of the formation of iron oxides, $\text{Fe}(\text{CO})_5$, and carbon oxides as a function of temperature at standard pressure. The Fe and coal have already undergone oxidation within this range of combustion temperatures. Gaseous FeO is thermodynamically unfavorable in this temperature range, whereas solid iron oxides, such as FeO(s) and Fe_2O_3 (s), are thermodynamically preferred. The CO resulting from the oxidation of CH_4 or coal may mix with the Fe particles and begin replacing O and yielding $\text{Fe}(\text{CO})_5$. In this context, $\text{Fe}(\text{CO})_5$ is thermodynamically preferred over iron oxides. In the present study, the Fe particles oxidized and expanded in size, and the CO

diffused inside the Fe particle shell, causing the heterogeneous formation of $\text{Fe}(\text{CO})_5$ across the inner surface. The thermal expansion and severe combustion of trapped CO and the produced $\text{Fe}(\text{CO})_5$ can be attributed to the Fe particle microexplosion.

4. Conclusions

This study investigated the combustion of micron-sized metal particles on a laboratory pilot-scale combustor. Three metal fuels—pure Fe, an Fe–Al mixture, and a Fe–coal mixture—were prepared and doped into a CH_4 –air premixed flame. The metal fuel concentration was key to the formation of a coupled flame front, and the particle feed rate of 46.48 g/m^3 was sufficient for all the tested fuels. Regarding the Fe–coal-doped flame, once the coal particles were ignited, they produced comet-tail-like traces in the flame. Only the Fe–Al-doped flame exhibited a strong bright flame cone, which can be ascribed to the homogeneous Al vapor reaction. The Fe–Al-doped flame with stronger flame front intensity had the highest flame temperature (1900 K). The temperatures of the Fe- and Fe–coal-doped flames ranged from 1600 to 1800 K.

Notably, numerous microexplosions occurred during Fe–coal combustion. We hypothesized that these microexplosions were caused by the formation of bubbles (a coalescence of $\text{Fe}(\text{CO})_5$ and oxygen) inside the thin agglomerate iron oxide shell. The bursting of the combustible $\text{Fe}(\text{CO})_5/\text{O}_2$ bubbles either expanded into thin-walled, hollow-shelled iron oxide products or fragmented the iron oxide products.

The combustion of metal fuels produced higher NO_x and fine particles; because of the high temperatures produced by the hybrid flame, the NO_x in the metal fuels mostly originated from thermal NO_x . A lower level of NO_x emission was observed in Fe–coal combustion and could be attributed to the radical scavenging effect of the inhibitor material, which was related to the thermal oxidation produced by $\text{Fe}(\text{CO})_5$. These emissions warrant consideration in future efforts pertaining to the use of metals as alternative energy carriers; therefore, the development of a posttreatment system is essential.

Declaration of Competing Interest

All authors declared that: (i) no support, financial or otherwise, has been received from any organization that may have an interest

in the submitted work; and (ii) there are no other relationships or activities that could appear to have influenced the submitted work.

Acknowledgments

This work was supported by the [Taiwan Ministry of Science and Technology](#) under grant numbers [MOST 108–2628-E-006–008-MY3](#) and [MOST 109–2221-E-006–037-MY3](#).

Supplementary materials

Supplementary material associated with this article can be found, in the online version, at doi:[10.1016/j.combustflame.2021.02.013](https://doi.org/10.1016/j.combustflame.2021.02.013).

References

- [1] K.h. Wedepohl, [The composition of the continental crust](#), *Geochimica et Cosmochimica Acta* 59 (1995) 1217–1232.
- [2] R.A. Yetter, G.A. Risha, S.F. Son, Metal particle combustion and nanotechnology, *Proc. Combust. Inst.* 32 (2) (2009) 1819–1838, doi:[10.1016/j.proci.2008.08.013](https://doi.org/10.1016/j.proci.2008.08.013).
- [3] N. Auner, S. Holl, Silicon as energy carrier—Facts and perspectives, *Energy* 31 (10–11) (2006) 1395–1402, doi:[10.1016/j.energy.2005.12.001](https://doi.org/10.1016/j.energy.2005.12.001).
- [4] S. Wang, A.L. Corcoran, E.L. Dreizin, Combustion of magnesium powders in products of an air/acetylene flame, *Combust. Flame* 162 (4) (2015) 1316–1325, doi:[10.1016/j.combustflame.2014.10.016](https://doi.org/10.1016/j.combustflame.2014.10.016).
- [5] C. Badiola, R.J. Gill, E.L. Dreizin, Combustion characteristics of micron-sized aluminum particles in oxygenated environments, *Combust. Flame* 158 (10) (2011) 2064–2070, doi:[10.1016/j.combustflame.2011.03.007](https://doi.org/10.1016/j.combustflame.2011.03.007).
- [6] R.J. Gill, C. Badiola, E.L. Dreizin, Combustion times and emission profiles of micron-sized aluminum particles burning in different environments, *Combust. Flame* 157 (11) (2010) 2015–2023, doi:[10.1016/j.combustflame.2010.02.023](https://doi.org/10.1016/j.combustflame.2010.02.023).
- [7] C. Griego, N. Yilmaz, A. Atmanli, Sensitivity analysis and uncertainty quantification on aluminum particle combustion for an upward burning solid rocket propellant, *Fuel* 237 (2019) 1177–1185, doi:[10.1016/j.fuel.2018.10.032](https://doi.org/10.1016/j.fuel.2018.10.032).
- [8] C. Griego, N. Yilmaz, A. Atmanli, Analysis of aluminum particle combustion in a downward burning solid rocket propellant, *Fuel* 237 (2019) 405–412, doi:[10.1016/j.fuel.2018.10.016](https://doi.org/10.1016/j.fuel.2018.10.016).
- [9] D.S. Sundaram, V. Yang, T.L. Connell, G.A. Risha, and R.A. Yetter, "Flame propagation of nano/micron-sized aluminum particles and ice (ALICE) mixtures", *Proc. Combust. Inst.*, vol. 34, no. 2, pp. 2221–2228, 2013, doi:[10.1016/j.proci.2012.06.129](https://doi.org/10.1016/j.proci.2012.06.129).
- [10] Y. Yang, M. He, Thermodynamic cycle analysis of ramjet engines using magnesium-based fuel, *Aerosp. Sci. Technol.* 22 (1) (2012) 75–84, doi:[10.1016/j.ast.2011.06.005](https://doi.org/10.1016/j.ast.2011.06.005).
- [11] J.M. Bergthorson, Recyclable metal fuels for clean and compact zero-carbon power, *Prog. Energy Combust. Sci.* 68 (2018) 169–196, doi:[10.1016/j.pecs.2018.05.001](https://doi.org/10.1016/j.pecs.2018.05.001).
- [12] J.M. Bergthorson, et al., Direct combustion of recyclable metal fuels for zero-carbon heat and power, *Appl. Energy* 160 (2015) 368–382, doi:[10.1016/j.apenergy.2015.09.037](https://doi.org/10.1016/j.apenergy.2015.09.037).
- [13] P. Julien, S. Whiteley, S. Goroshin, M.J. Soo, D.L. Frost, J.M. Bergthorson, Flame structure and particle-combustion regimes in premixed methane–iron–air suspensions, *Proc. Combust. Inst.* 35 (2) (2015) 2431–2438, doi:[10.1016/j.proci.2014.05.003](https://doi.org/10.1016/j.proci.2014.05.003).
- [14] J.-H. Sun, R. Dobashi, T. Hirano, Structure of flames propagating through metal particle clouds and behavior of particles, *Symp. (Int.) Combust.* 27 (2) (1998) 2405–2411 /01/01/1998, doi:[10.1016/S0082-0784\(98\)80092-1](https://doi.org/10.1016/S0082-0784(98)80092-1).
- [15] F.-D. Tang, S. Goroshin, A.J. Higgins, Modes of particle combustion in iron dust flames, *Proc. Combust. Inst.* 33 (2) (2011) 1975–1982 /01/01/2011, doi:[10.1016/j.proci.2010.06.088](https://doi.org/10.1016/j.proci.2010.06.088).
- [16] K.-L. Chintersingh, M. Schoenitz, E.L. Dreizin, Combustion of boron and boron-iron composite particles in different oxidizers, *Combust. Flame* 192 (2018) 44–58 /06/01/2018, doi:[10.1016/j.combustflame.2018.01.043](https://doi.org/10.1016/j.combustflame.2018.01.043).
- [17] K.-L. Chintersingh, M. Schoenitz, E.L. Dreizin, Boron doped with iron: preparation and combustion in air, *Combust. Flame* 200 (2019) 286–295 /02/01/2019, doi:[10.1016/j.combustflame.2018.11.031](https://doi.org/10.1016/j.combustflame.2018.11.031).
- [18] S.A. Hashim, P.K. Ojha, S. Karmakar, A. Roy, D. Chaira, Experimental observation and characterization of B–HTPB-based solid fuel with addition of iron particles for hybrid gas generator in ducted rocket applications, *Propellants Explos. Pyrotech.* 44 (7) (2019) 896–907, doi:[10.1002/prep.201900009](https://doi.org/10.1002/prep.201900009).
- [19] M.D. Grapes, R.V. Reeves, K. Fezzaa, T. Sun, J.M. Densmore, K.T. Sullivan, In situ observations of reacting Al/Fe₂O₃ thermite: relating dynamic particle size to macroscopic burn time, *Combust. Flame* 201 (2019) 252–263 /03/01/2019, doi:[10.1016/j.combustflame.2018.12.021](https://doi.org/10.1016/j.combustflame.2018.12.021).
- [20] K.T. Sullivan, M.A. Worsley, J.D. Kuntz, A.E. Gash, Electrophoretic deposition of binary energetic composites, *Combust. Flame* 159 (6) (2012) 2210–2218 /06/01/2012, doi:[10.1016/j.combustflame.2012.01.021](https://doi.org/10.1016/j.combustflame.2012.01.021).
- [21] G.M. Dutro, R.A. Yetter, G.A. Risha, S.F. Son, The effect of stoichiometry on the combustion behavior of a nanoscale Al/MoO₃ thermite, *Proc. Combust. Inst.* 32 (2) (2009) 1921–1928 /01/01/2009, doi:[10.1016/j.proci.2008.07.028](https://doi.org/10.1016/j.proci.2008.07.028).
- [22] J.M. Densmore, K.T. Sullivan, A.E. Gash, J.D. Kuntz, Expansion behavior and temperature mapping of thermites in burn tubes as a function of fill length, *Propell. Explos. Pyrotech.* 39 (3) (2014) 416–422 /06/01/2014, doi:[10.1002/prep.201400024](https://doi.org/10.1002/prep.201400024).
- [23] M.R. Weismiller, J.Y. Malchi, J.G. Lee, R.A. Yetter, T.J. Foley, Effects of fuel and oxidizer particle dimensions on the propagation of aluminum containing thermites, *Proc. Combust. Inst.* 33 (2) (2011) 1989–1996 /01/01/2011, doi:[10.1016/j.proci.2010.06.104](https://doi.org/10.1016/j.proci.2010.06.104).
- [24] E.R. Wainwright, T.A. Schmauss, S. Vummidi Lakshman, K.R. Overdeep, T.P. Weihs, Observations during Al:Zr composite particle combustion in varied gas environments, *Combust. Flame* 196 (2018) 487–499, doi:[10.1016/j.combustflame.2018.06.026](https://doi.org/10.1016/j.combustflame.2018.06.026).
- [25] Y. Feng, L. Ma, Z. Xia, L. Huang, D. Yang, Ignition and combustion characteristics of single gas-atomized Al–Mg alloy particles in oxidizing gas flow, *Energy* 196 (2020) 117036, doi:[10.1016/j.energy.2020.117036](https://doi.org/10.1016/j.energy.2020.117036).
- [26] J. Yu, et al., Combustion behaviors and flame microstructures of micro- and nano-titanium dust explosions, *Fuel* 181 (2016) 785–792, doi:[10.1016/j.fuel.2016.05.085](https://doi.org/10.1016/j.fuel.2016.05.085).
- [27] E.L. Dreizin, W. Felder, D.G. Keil, Phase changes in boron ignition and combustion, *Combust. Flame* 119 (1999) 272–290.
- [28] C. Badiola, E. Dreizin, Combustion of micron-sized particles of titanium and zirconium, *Proc. Combust. Inst.* 34 (2013) 2237–2243.
- [29] S.V.L. Elliot R. Wainwright, A.F.T. Leonga, A.H. Kinseya, J.D. Gibbins, S.Q. Arlington, T. Sun, K. Fezzaa, T.C. Hufnagel, T.P. Weihs, Viewing internal bubbling and microexplosions in combusting metal particles via x-ray phase contrast imaging, *Combust. Flame* 199 (2019) 194–203.
- [30] J.M. Bergthorson, M.J. Thomson, A review of the combustion and emissions properties of advanced transportation biofuels and their impact on existing and future engines, *Renew. Sustain. Energy Rev.* 42 (2015) 1393–1417, doi:[10.1016/j.rser.2014.10.034](https://doi.org/10.1016/j.rser.2014.10.034).
- [31] C.-W. Huang, Y.-H. Li, K.-L. Xiao, J. Lasek, Cofiring characteristics of coal blended with torrefied Miscanthus biochar optimized with three Taguchi indexes, *Energy* 172 (2019) 566–579 /04/01/2019, doi:[10.1016/j.energy.2019.01.168](https://doi.org/10.1016/j.energy.2019.01.168).
- [32] Y.-H. Li, W.-C. Kuo, The study of optimal parameters of oxygen-enriched combustion in fluidized bed with optimal torrefied woody waste, *Int. J. Energy Res.* 44 (9) (2020) 7416–7434, doi:[10.1002/er.5459](https://doi.org/10.1002/er.5459).
- [33] E.N. Lysenko, A.P. Surzhikov, S.P. Zhuravkov, V.A. Vlasov, A.V. Pustovalov, N.A. Yavorovskiy, The oxidation kinetics study of ultrafine iron powders by thermogravimetric analysis, *J. Therm. Anal. Calorim.* 115 (2) (2013) 1447–1452, doi:[10.1007/s10973-013-3456-x](https://doi.org/10.1007/s10973-013-3456-x).
- [34] R.Y. Chen, W.Y.D. Yeun, Review of the high-temperature oxidation of iron and carbon steels in air or oxygen, *Oxid. Met.* 59 (2003) 433–468.
- [35] E.L. Dreizin, Metal-based reactive nanomaterials, *Prog. Energy Combust. Sci.* 35 (2) (2009) 141–167 /04/01/2009, doi:[10.1016/j.pecs.2008.09.001](https://doi.org/10.1016/j.pecs.2008.09.001).
- [36] M.A. Trunov, M. Schoenitz, X. Zhu, E.L. Dreizin, Effect of polymorphic phase transformations in Al₂O₃ film on oxidation kinetics of aluminum powders, *Combust. Flame* 140 (4) (2005) 310–318 /03/01/2005, doi:[10.1016/j.combustflame.2004.10.010](https://doi.org/10.1016/j.combustflame.2004.10.010).
- [37] E.L. Dreizin, Experimental study of stages in aluminum particle combustion in air, *Combust. Flame* 105 (4) (1996) 541–556, doi:[10.1016/0010-2180\(95\)00224-3](https://doi.org/10.1016/0010-2180(95)00224-3).
- [38] P. Glarborg, J.A. Miller, B. Ruscic, S.J. Klippenstein, Modeling nitrogen chemistry in combustion, *Prog. Energy Combust. Sci.* 67 (2018) 31–68, doi:[10.1016/j.pecs.2018.01.002](https://doi.org/10.1016/j.pecs.2018.01.002).
- [39] A. Raj, E. Croiset, J.Z. Wen, Numerical analysis of effects of iron pentacarbonyl as fuel additive for reducing NO and soot precursors from methane/air diffusion flame, *Fuel* 216 (2018) 768–780, doi:[10.1016/j.fuel.2017.12.013](https://doi.org/10.1016/j.fuel.2017.12.013).
- [40] L.P.H. Jeurgens, F.D. Tichelaar, E.J. Mittemeijer, W.G. Sloof, Structure and morphology of aluminium-oxide films formed by thermal oxidation of aluminium, *Thin Solid Films* 418 (2002) 89–101.
- [41] L.P.H. Jeurgens, W.G. Sloof, F.D. Tichelaar, E.J. Mittemeijer, Thermodynamic stability of amorphous oxide films on metals: application to aluminum oxide films on aluminum substrates, *Phys. Rev. B* 62 (7) (2000) 4707–4719, doi:[10.1103/PhysRevB.62.4707](https://doi.org/10.1103/PhysRevB.62.4707).
- [42] R.W. Gurry, L.S. Darken, The system iron–oxygen. II. equilibrium and thermodynamics of liquid oxide and other phases, *J. Am. Chem. Soc.* 68 (5) (1946) 798–816 May 11946, doi:[10.1021/ja01209a030](https://doi.org/10.1021/ja01209a030).
- [43] M.W. Chase Jr., NIST-JANAF thermochemical tables, *J. Phys. Chem. Ref. Data*, Monograph 9 (1998) <https://janaf.nist.gov/>.